remote sensing

MDPI

Letter

Mapping, Monitoring, and Prediction of Floods Due to Ice Jam and Snowmelt with Operational Weather Satellites

Mitchell D. Goldberg [1], Sanmei Li [2], Daniel T. Lindsey [3], William Sjoberg [1], Lihang Zhou [1] and Donglian Sun [2,*]

[1] NOAA JPSS Program Office, Lanham, MD 20706, USA; mitch.goldberg@noaa.gov (M.D.G.); bill.sjoberg@noaa.gov (W.S.); Lihang.Zhou@noaa.gov (L.Z.)
[2] Department of Geography and Geo-Information Science, George Mason University, Fairfax, VA 22030, USA; slia@gmu.edu
[3] NOAA/NESDIS Senior Scientific Adviser for GOES-R, Fort Collins, CO 80523, USA; dan.lindsey@noaa.gov
* Correspondence: dsun@gmu.edu; Tel.: +1-703-993-4736

Received: 7 May 2020; Accepted: 3 June 2020; Published: 9 June 2020

Abstract: Among all the natural hazards throughout the world, floods occur most frequently. They occur in high latitude regions, such as: 82% of the area of North America; most of Russia; Norway, Finland, and Sweden in North Europe; China and Japan in Asia. River flooding due to ice jams may happen during the spring breakup season. The Northeast and North Central region, and some areas of the western United States, are especially harmed by floods due to ice jams and snowmelt. In this study, observations from operational satellites are used to map and monitor floods due to ice jams and snowmelt. For a coarse-to-moderate resolution sensor on board the operational satellites, like the Visible Infrared Imaging Radiometer Suite (VIIRS) on board the National Polar-orbiting Partnership (NPP) and the Joint Polar Satellite System (JPSS) series, and the Advanced Baseline Imager (ABI) on board the GOES-R series, a pixel is usually composed of a mix of water and land. Water fraction can provide more information and can be estimated through mixed-pixel decomposition. The flood map can be derived from the water fraction difference after and before flooding. In high latitude areas, while conventional observations are usually sparse, multiple observations can be available from polar-orbiting satellites during a single day, and river forecasters can observe ice movement, snowmelt status and flood water evolution from satellite-based flood maps, which is very helpful in ice jam determination and flood prediction. The high temporal resolution of geostationary satellite imagery, like that of the ABI, can provide the greatest extent of flood signals, and multi-day composite flood products from higher spatial resolution imagery, such as VIIRS, can pinpoint areas of interest to uncover more details. One unique feature of our JPSS and GOES-R flood products is that they include not only normal flood type, but also a special flood type as the supra-snow/ice flood, and moreover, snow and ice masks. Following the demonstrations in this study, it is expected that the JPSS and GOES-R flood products, with ice and snow information, can allow dynamic monitoring and prediction of floods due to ice jams and snowmelt for wide-end users.

Keywords: ice jam; snowmelt; flood mapping; monitoring and prediction; VIIRS; ABI

1. Introduction

Floods are the most frequent natural hazard throughout the world. The regions where river flooding due to ice jams may happen, during the spring breakup season, include: 82% of the area of North America, including the whole of Canada and 52% of the United States; most of Russia; Norway, Finland, and Sweden in North Europe; China and Japan in Asia [1]; and other morphological areas,

like in the alpine valleys [2]. In the United States, floods cause the highest amount of life and economic loss among all the severe weather events [3]. Floods caused by snow/ice melting occur almost every year in the United States, for example, severe floods occurred along the Red River in April 2020, spring 2014, April 2013, March 2010 and April 2006. The Northeast and North Central United States are especially effected by floods due to ice jam and snowmelt. Although most flood events caused by ice jams and snowmelt are relatively minor and only affect local areas, a high number of significant floods related to ice jam and snowmelt have caused severe property damage and deaths.

The National Weather Service can issue routine river flood outlooks and warnings in the United States, but there is currently no widespread way to determine flood extent over land resulting from snowmelt and ice jams. Due to the complexity of river ice processes and thermal rises, and the relative predisposition to melts or instability effects in mountain areas, modeling floods due to ice jams and snowmelt is more complicated than modeling open-water flood [4–7]. Although numerical models have been developed for ice floods in several rivers all over the world [8–11], these were mainly designed for simulation, and rarely for prediction [4,11]. Yu et al. [12] indicates that the uncertainties in ice thermal and flow conditions inhibit the predictive capability of hydraulic/river ice models.

Satellite remote sensing provides a useful approach to detecting, determining and estimating the flood extent, as well as damage and impact over rivers and land bodies [13–15]. Operational weather satellites can provide ideal tools for flood detection, because of their large spatial coverage, frequent observations, low cost, and ease in distinguishing between water and land. During the daytime, flood maps can be derived from optical sensors onboard the operational weather satellites, such as visible (VIS), near-infrared (NIR) [13–15] and shortwave-infrared (SWIR) [16] observations under clear sky conditions. Due to their capacity to penetrate non-rainy clouds, microwave remote sensing instruments, including active airborne synthetic aperture radar (SAR) imagery [17] and passive microwave (MW) instruments [18–22], and especially SAR with high spatial resolution (10–30 m), if available, can provide invaluable flood information under almost all weather conditions. Nevertheless, SAR usually has a narrow swath and long revisit time (6–12 days) [17], while a flood is often a short-term event. Meanwhile, passive MW sensors usually have very coarse spatial resolutions (10–25 km) [18–22]. Optical sensors can explain surface flood information straightforwardly, with simpler preprocessing.

Remote sensing demonstrates great potential for monitoring river ice conditions [23]. Moderate Resolution Imaging Spectroradiometer (MODIS) and RADARSAT-2 were used to detect unbroken ice cover, monitor ice cover conditions and estimate ice volume [24,25]. The large spatial coverage and frequent observations of operational weather satellites, like the Suomi National Polar-Orbiting Partnership (S-NPP) and the Joint Polar Satellite System (JPSS) series, have unique advantages for flood monitoring. The S-NPP and JPSS constellation allows the Alaskan region to receive low latency data from 28 daily overpasses [26]. For high latitude regions, the revisit time is about 50–90 min, depending on latitudes and locations. Since in high latitude regions conventional observation is sparse, the capacity for multiple observations from operational polar-orbiting satellites during the daytime makes the Visible Infrared Imaging Radiometer Suite (VIIRS) onboard the S-NPP and JPSS series very attractive for flood monitoring. These floods can be tracked dynamically by VIIRS in near-real time, which can thus be used for early warning and loss assessment by users from river forecast centers.

Floods caused by snowmelt and ice jams occur almost every year in the United States, and notable scenarios include the floods that happened along the Yukon River and Koyukuk River in Alaska in May–June 2013 due to ice jams, and the significant flooding that occurred along the Red River, recently, in April 2020. In order to meet the needs from end users, in this study, the S-NPP VIIRS 375-m and GOES-R imager data are used to detect floods caused by ice jams and snowmelt. Here we demonstrate an application of our flood algorithm in ice jam flood monitoring, and an application for snowmelt flood detection.

2. Data and Methods

2.1. Study Sites

The Yukon River is the third longest river in North America and the longest river in Yukon, Alaska. The river originates from British Columbia, Canada, and flows west to Alaska in the United States. Ice jams and flooding are very common on the Yukon River when warming temperatures in spring melt the ice. In May 2013, a persistent ice jam on the Yukon River overtopped its banks and carried flooding water to the town of Galena in Alaska. Since then, there has been no real big ice jam flood till now. The location of the Yukon River is marked in Figure 1.

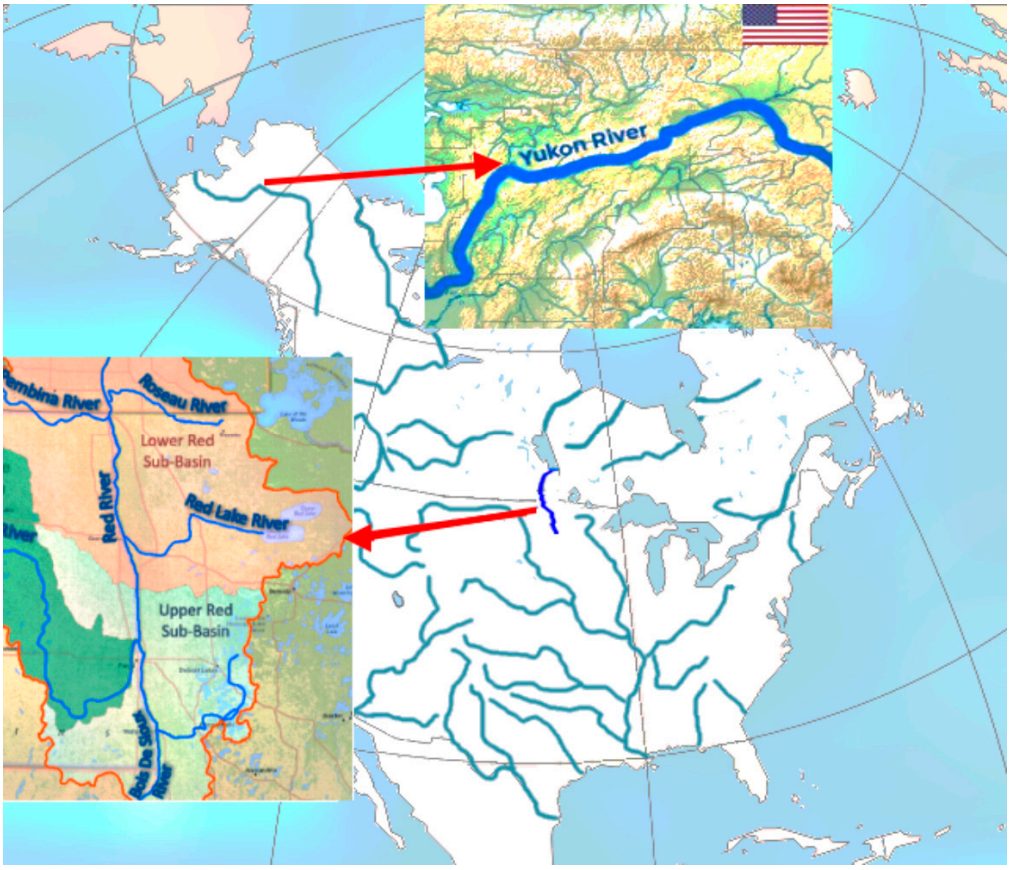

Figure 1. The location map of the study sites in the United States. The thick blue lines mark the major rivers in North America.

The Red River flows northward, along the border of North Dakota and Minnesota, in the United States, through Manitoba, Canada. The Red River passes through several cities, including Fargo and Grand Forks in the United States, and Manitoba's capital, Winnipeg in Canada. Water draining northeast on a gentle slope was dammed by the south edge of the continental ice sheet. In spring, the Red River thaws first from the south in North Dakota, while still frozen farther north, causing widespread flooding. The location of the Red River is showed in Figure 1.

2.2. Data Used

To estimate the flooding caused by ice jam and snowmelt, S-NPP VIIRS, GOES-R Advanced Baseline Imager (ABI) and other types of ancillary data were used:

1. Calibrated VIIRS level 1b data at imagery channel 1 (red: 600–680 nm), channel 2 (near-infrared: 850–880 nm), channel 3 (shortwave infrared: 1610 nm), and thermal infrared channel 5 (1050–1240 nm) with 375-m spatial resolution.

2. The calibrated level 1b GOES-16 ABI near real-time data
3. GOES-R and VIIRS geolocation data, including longitude, latitude, solar zenith angles, solar azimuth angles, sensor zenith angles and sensor azimuth angles.
4. S-NPP/VIIRS cloud mask Intermediate Product at 750-m resolution
5. M-band terrain-corrected geolocation data (GMTCO).
6. The National Land Cover Database 2006 (NLCD) of the United States Geological Survey (USGS) [27].
7. Linear hydrographic feature data, including major rivers, streams and canals, and area hydrographic feature data, including major lakes and reservoirs.
8. MODIS 250-m global water mask (MOD44W) [28,29].

2.3. Methods

2.3.1. Flooding Water Detection

Because of different underlying surface conditions, there are two primary types of floods: the most common flood occurs over vegetation or bare land, referred to as supra-vegetation/bare land flood; another flood type mainly occurs on top of snow/ice surfaces, referred to as supra-snow/ice flood. These two types of floods show different spectral characteristics in optical sensor observations, in visible, near infrared, shortwave infrared and thermal infrared channels, and thus require different methodologies for flood detection using optical sensor data, like the VIIRS imagery.

The supra-snow/ice flood is a special flood type because the underlying layer is still covered with snow/ice. Because the reflectance of snow and ice is high, floodwater over a snow/ice surface reflects much more in visible (VIS) and near infrared (NIR) channels than floodwater in normal supra-vegetation/bare land floods, while the reflectance in the visible channel (R_{Vis}) is still higher than in the NIR channel (R_{NIR}) [30–32]. The detection of supra-snow snow/ice flood also uses similar variables: R_{Vis}, R_{NIR} and NDVI (or Normalized Difference Vegetation Index). However, the melting snow/ice surface and shadows cast on the snow/ice surface share similar spectral features in these three variables, and thus may be confused with supra-snow/ice floodwater. We therefore introduce a new variable, DNDVI, defined as the Difference in NDVI between a pixel and its snow/ice neighbors. As demonstrated in Li et al. [33], shadows on snow and melting snow surfaces have similar R_{Vis}, R_{NIR} and NDVI values, while melting snow and shadows can be separated from supra-snow/ice floodwater using the DNDVI value.

For supra-snow/ice floods, VIIRS snow/ice mask is applied before flood detection to determine snow/ice cover. The decision-tree technique is used to distinguish supra-snow/ice floodwater from snow/ice cover and shadows based on these variables: reflectance in the visible channel R_{VIS}, NDVI and DNDVI [28].

2.3.2. Cloud Shadow Removal

For flood detection, cloud shadow is always the biggest challenge because cloud shadows share very similar spectral characteristic with flooding water in the visible, near infrared, short-wave infrared and thermal infrared channels, meaning these cannot be separated from one another via spectral characteristics. Thus, during water detection based on the decision-tree approach, most cloud shadows are counted as water. To remove these cloud shadows from flooding water pixels, we evaluated the cloud shadow results in cloud masks and applied them in cloud shadow removal first. Then we adjust the geometric cloud shadow removal algorithm [34] for VIIRS imagery. This method made an assumption that one cloud pixel casts, at most, one cloud shadow pixel. A spherical geometry model between cloud shadows and clouds is developed, and cloud height is required. To avoid possible errors in cloud height products, the geometry model is applied iteratively to build the cloud-to-shadow relationship. By adjusting the geometric cloud shadow removal algorithm, further improvements can be made to solve the remaining cirrus-cloud shadows [34].

2.3.3. Terrain Shadow Removal

Terrain shadow is another big challenge in flood detection, because terrain shadows also show similar reflectance properties to water, and may be misclassified as flooding water. To remove terrain shadows, an object-based method is developed using the digital elevation model (DEM) data, resampled to VIIRS or GOES-R resolution from the Shuttle Radar Topography Mission (SRTM)-2 and Advanced Spaceborne Thermal Emission and Reflection Radiometer (ASTER) [35]. Since terrain shadows usually form in mountainous areas while flooding water mainly accumulates in low-lying areas, the surface roughness of terrain shadows is much greater than that of floodwater [36]. Instead of working on single pixels, this object-based method treats a group of adjacent pixels as one object to calculate surface roughness.

The method was applied to identify terrain shadows in the VIIRS-derived flood maps. The validation results show that more than 95% of the terrain shadows can be separated from the flooding water, and some of the remaining cloud shadows can also be removed [35].

2.3.4. Flooding Water Fraction Derivation

Since a flood is the overflowing of water onto normally dry land area, for a coarse-to-moderate resolution sensor like VIIRS and ABI, flooded pixels may be mixed with water and land. Thus, the flooding water fraction can represent mixed pixel information, and contain more information than just "yes/no" flood water mask [9], as in the most common satellite-based flood mapping. Therefore, after water classification, if a pixel is classified as "Water", we further calculate its water fraction based on the linear mixture model [16]:

$$f_w = \frac{R_{ch\_land} - R_{ch\_mix}}{R_{ch\_land} - R_{ch\_water}} \quad (1)$$

where f_w is the water fraction, R_{ch_mix} is the reflectance for mixed pixels, R_{ch_land} is the reflectance for pure land pixels and R_{ch_water} is the reflectance for pure water pixels. The reflectance in the visible (VIS) channel (e.g., VIIRS Imagery Band 1 or I1: 0.64 μm), near IR (NIR) channel (e.g., VIIRS Imagery Band 2 or I2: 0.865 μm) and shortwave IR (*SWIR*) channel (e.g., VIIRS Imagery Band 3 or I3: 1.61 μm) are used. As a land pixel may be any surface type (like vegetation, grass, bare land, etc.), R_{ch_land} values vary for different surface types. In order to find the exact threshold values, especially the R_{ch_land} for land end members, a dynamic nearest neighbor searching (DNNS) method was developed to dynamically search the nearby land and water end members [16]:

$$\begin{array}{c} \frac{R_{vis\_mix}}{R_{SWIR\_mix}} - \frac{R_{vis\_water}}{R_{SWIR\_mix}} < \frac{R_{vis\_land}}{R_{SWIR\_land}} < \frac{R_{vis\_mix}}{R_{SWIR\_mix}} \\ \frac{R_{NIR\_mix}}{R_{SWIR\_mix}} - \frac{R_{NIR\_water}}{R_{SWIR\_mix}} < \frac{R_{NIR\_land}}{R_{SWIR\_land}} < \frac{R_{NIR\_mix}}{R_{SWIR\_mix}} \end{array} \quad (2)$$

Equations (2) provide the basis for finding the nearby pure land and water pixels, which are searched in a dynamic window (100 × 100 pixels) around each mixed pixel. The nearest pure land and water pixels that satisfy the relationship described in Equations (2) are located in the loop, the average reflectance of all the identified land pixels is taken as R_{ch_land}, and the average channel reflectance of all the found water pixels is used as the reflectance of pure water (R_{ch_water}). The water fraction can then be calculated from Equation (1). Based on the difference in the water fraction after and before flooding, a flood map can be derived. The algorithm process flowchart can be found in Li et al. [33].

3. Results

High latitude areas in North America may suffer from floods due to ice jams, especially during spring break up season. Here we show an example of a disastrous flood caused by an ice jam along the Yukon River in Alaska from, 27 May to early June, 2013.

The algorithms described above were applied to the Suomi-NPP/VIIRS data to map and monitor the flooding process dynamically. The flood detection is performed with the water detection and fraction products at the original 375-m resolution.

Figure 2 shows the VIIRS false color image and the corresponding flood detection map at 20:27 Coordinated Universal Time (UTC) on 27 May 2013. A long segment of the Yukon River near Galena was still covered with ice. Ice in the eastern section was mostly melted. Water flowed out of the riverbed to the east of Galena due to the ice jam. The flood could be identified from the VIIRS false color images. With the flood detection algorithms developed in this study, flooding water was detected at water fractions from 60% to 100%. At this time, the flooding water was confined to a small area, and city of Galena was still safe.

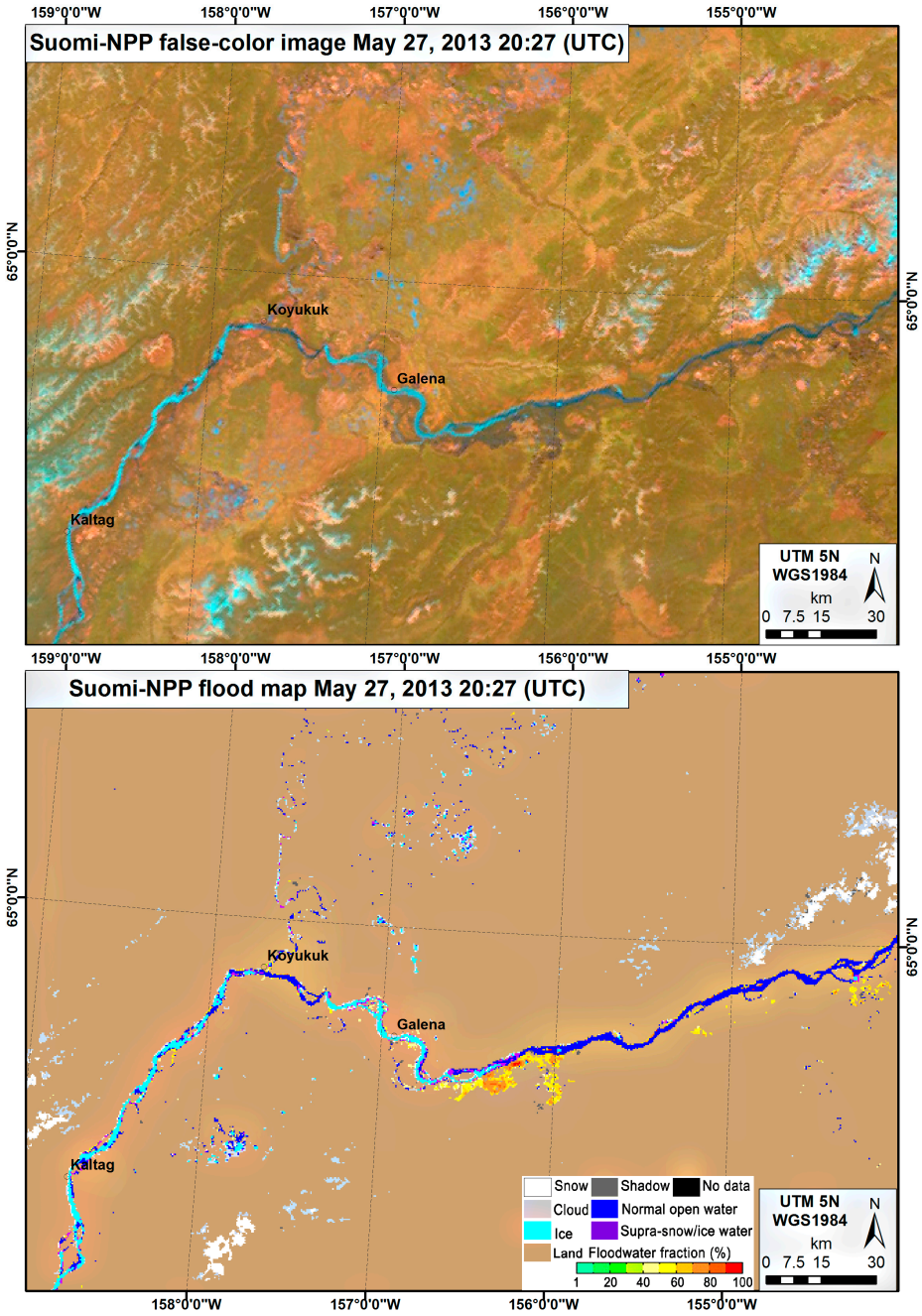

Figure 2. VIIRS false color image (**upper**) and the corresponding flood detection map (**lower**) along the Yukon River in Alaska on 27 May 2013.

The largest flooding occurred at 21:29 UTC on May 29 (Figure 3). Most of the flooding water fractions near Galena were close to 100%. Figure 3 shows VIIRS data with large areas of flooding water near Galena. The largest area of the flood was estimated to be approximately 18 miles long. In addition to the flooding along the Yukon River, flooding also occurred along the Koyukuk River because of an ice jam. Afterwards, the downstream ice melted gradually, and the flood water then began to retreat. Comparisons of visual analyses with the VIIRS false color images show a good consistency in the flood detection results (Figures 2 and 3). VIIRS flood maps can be generated automatically at near-real time, and are quantitative and more objective than using visual analysis in flood detection.

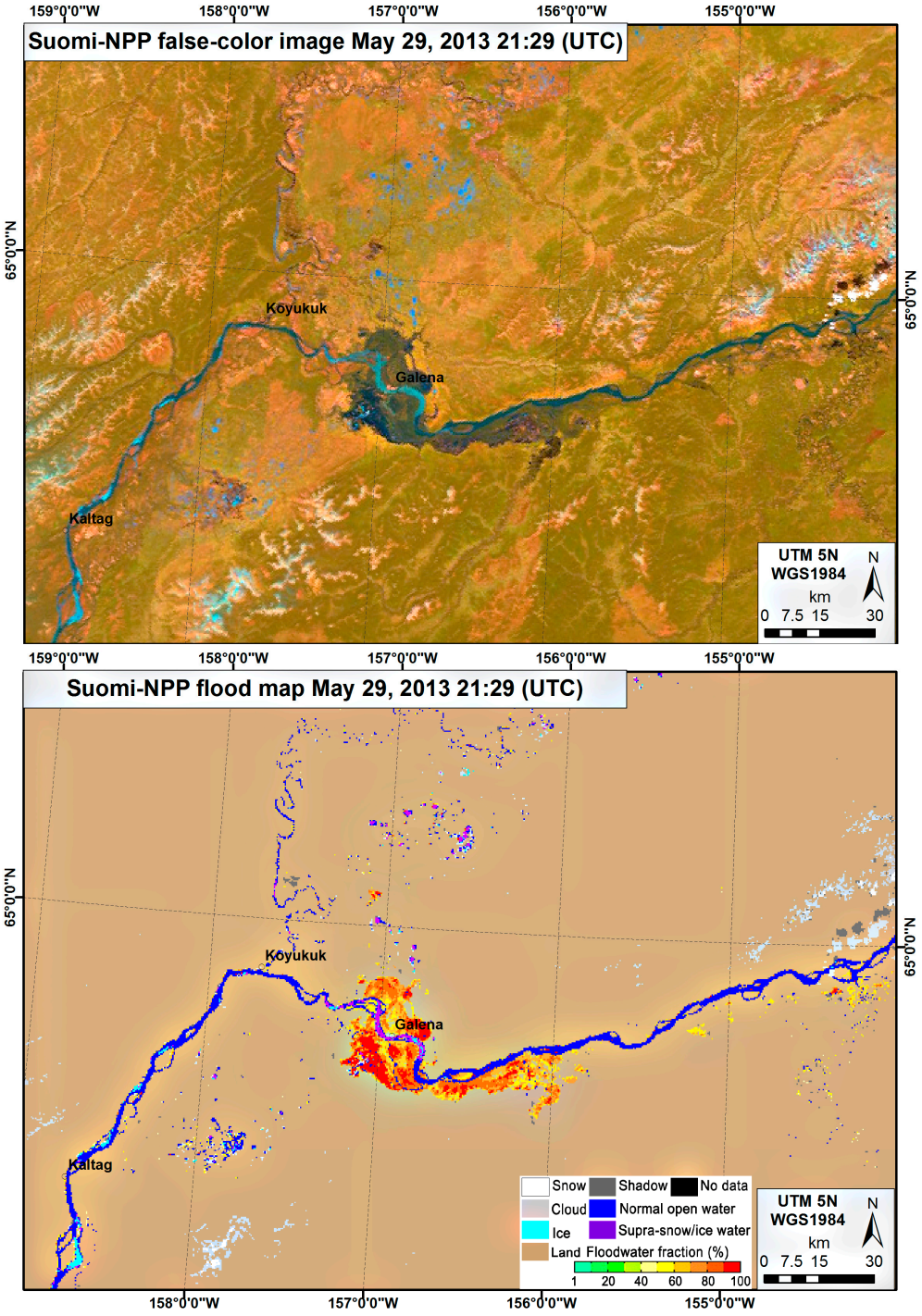

Figure 3. VIIRS false color image (**upper**) and the corresponding flood detection map (**lower**) along the Yukon River near Galena in Alaska on 29 May 2013.

One advantage of polar-orbiting satellites in high latitude regions is that multiple observations can be made available during a single day, which can thus help dynamically monitor and predict floods due to ice jams. Figure 4 further shows the formation regarding the ice jam flood near Galena, Alaska. We can see how ice jams can be determined by observing ice movement and flooding water evolution. In this figure, green arrows show the current ice location, yellow arrows mark the latest ice location, and red arrows identify the ice jam locations. We can see over a high latitude region, like Alaska, polar-orbiting satellite can provide multiple observations during a day. This is especially very helpful for tracking ice movement. We can see that within two hours, from 20:45 UTC to 22:27 UTC, on May 26, ice moved 8.9 km downstream along the Yukon River. From 22:25 UTC on May 26 to 20:27 UTC on May 27, ice moved 62.4 km further downstream within one day. Meanwhile, ice melted and became flooding water. The flooding progressed rapidly. Over less than 2 hours, from 20:27 UTC to 22:04 UTC, on the same May 27, ice moved further downstream 11.2 km toward the city of Galena. Late in the night of May 27, the flooding waters increased and the melting ice flowed downstream along the Yukon River, and most of Galena was under water by the morning of May 28 (Figure 4). The residents of Galena were forced to evacuate.

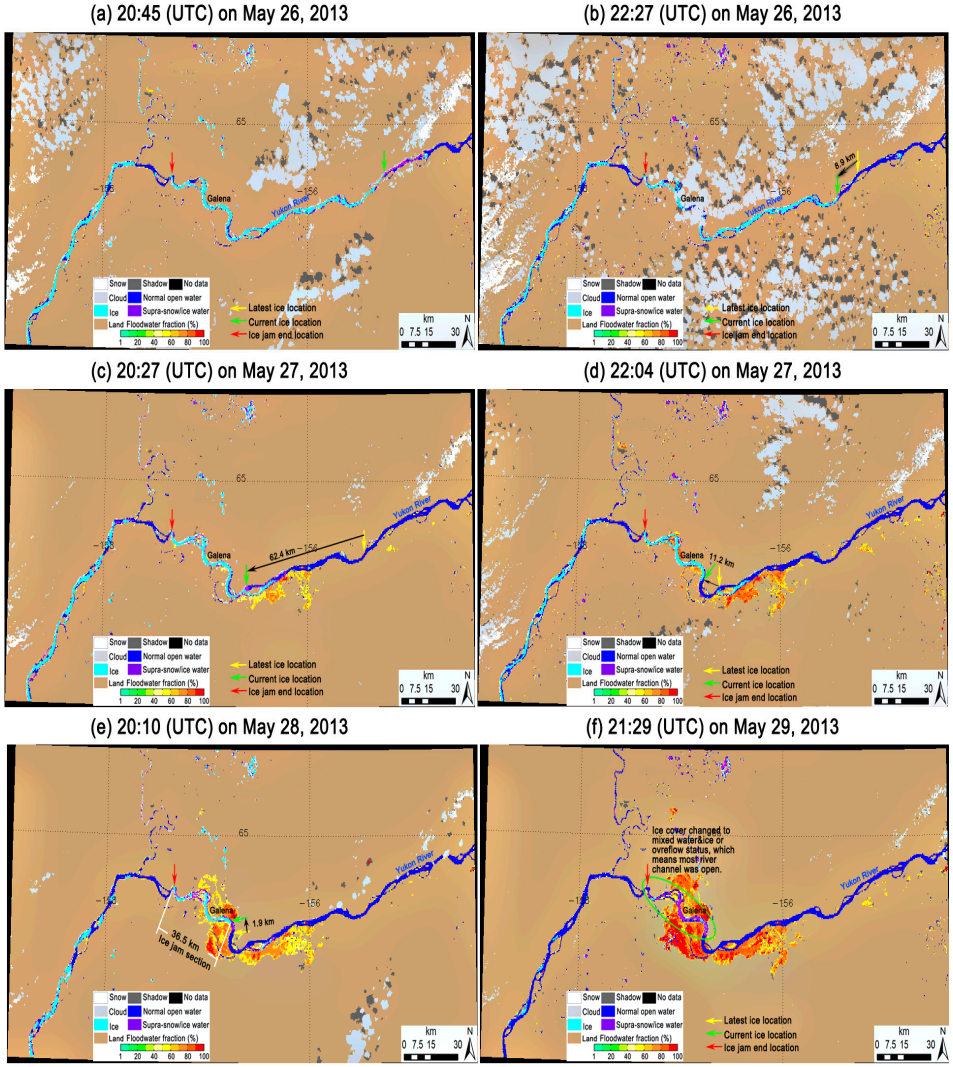

Figure 4. The flood detection maps at 20:45 UTC (**a**) and 22:27 UTC (**b**) on May 26; and at 20:27 UTC (**c**) and 22:04 UTC (**d**) on May 27, 20:10 UTC on May 28 (**e**) and 21:29 UTC on May 29 (**f**), 2013. Yellow arrow displays the latest ice location, green arrow indicates current ice location, and red arrow marks the ice jam location.

Figure 4e,f further shows the formation and retreat of the ice jam flood near Galena, AK, from 28 to 29 May 2013. With the multiple available observations, ice movement and flooding water evolution can be tracked. We can see that from 22:04 UTC on May 27 to 20:10 UTC on May 28, ice moved downstream another 1.9 km, along the Yukon River. Meanwhile, we can see the 36.5-km-long ice jam section. At 21:29 UTC on May 29, the ice cover changed to mixed water and ice, or to overflow status, and this means most of the river channel was open and the floodwater reached the maximum extent. Later, flooding waters decreased substantially, and retreated by 1 June 2013 (not shown).

The VIIRS and GOES-R flood products with ice and snow information can also be used to detect and monitor flood due to snowmelt, as shown in Figures 5 and 6. Figure 5 demonstrates how snow gradually melted and became flooding waters. The Red River flows from south to north toward colder latitudes, where ice jams tend to block the flow during the spring thaw season. Flooding within the Red River is a yearly signal of the end of winter and coming of summer. Spring of 2020 is proving to be no different; with major flooding occurring over much of the Red River and its tributaries due to seasonal snowmelt, the flood-prone river overtopped its banks again.

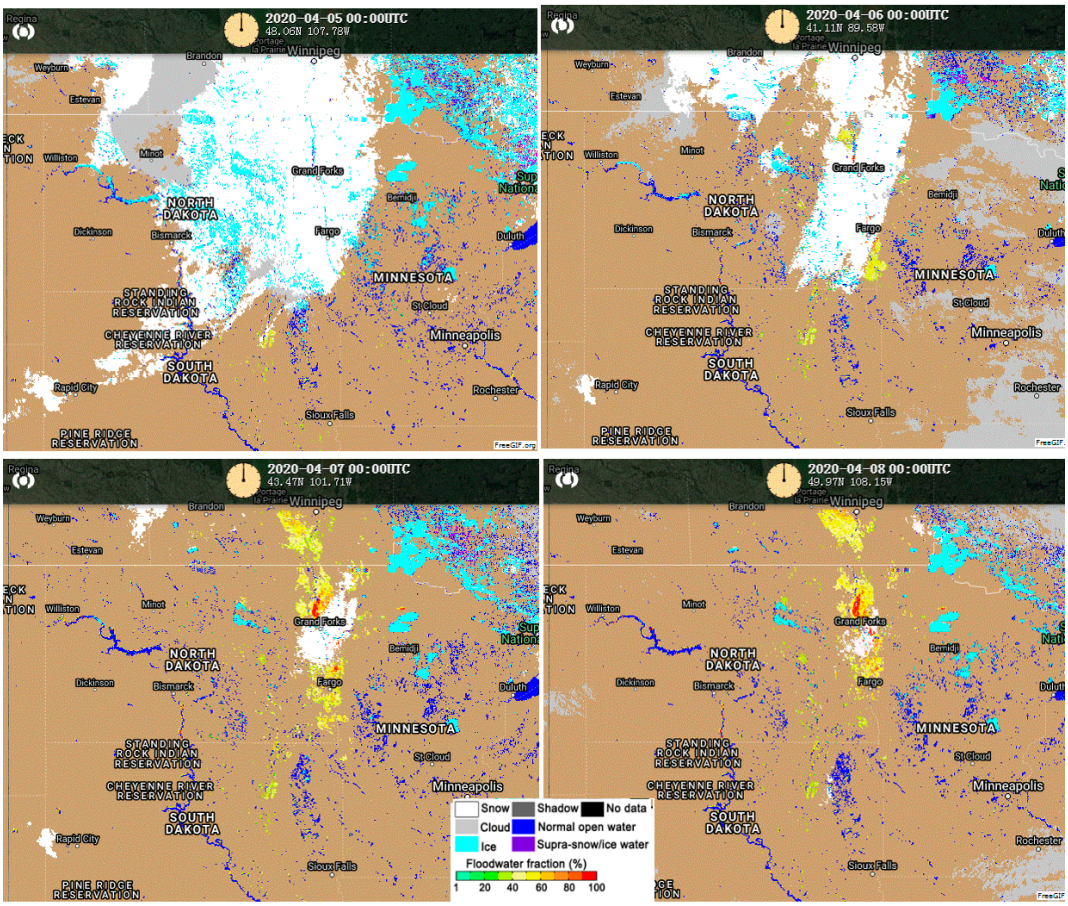

Figure 5. GOES-R ABI Flood Extent Product on April 5 (**a**), 6 (**b**), 7 (**c**) and 8 (**d**), 2020.

Wondering if there were any areas experiencing impactful flooding outside of the current NOAA (or National Oceanic and Atmospheric Administration) flood warnings, forecasters turned to GOES-R and VIIRS flood products for help in highlighting areas of observed floodwater coverage. Although GOES-R ABI is also an optical sensor, its high temporal resolution (5 min) enables it to capture some clear sky observations, allowing the possibility of observing floods during the day [37]. Figure 5 demonstrates GOES-R ABI flood products from 5 to 8 April 2020, when moderate-to-major flooding was occurring along the Red River and its tributaries within the central and northern basin, due to gradual snowmelt. In this figure, snow is marked as white and ice is represented by the cyan color.

Values higher than 60% (orange and red coloring) were of particular interest, and lower values into the 30–50% range were believed to be non-impactful standing meltwater. On April 5, there was still some snow along the Red River region. On April 6, snow started melting. On April 7, snow further melted and resulted in flooding, and on the next day, on April 8, snow continued to melt, and the flood extent area increased even more.

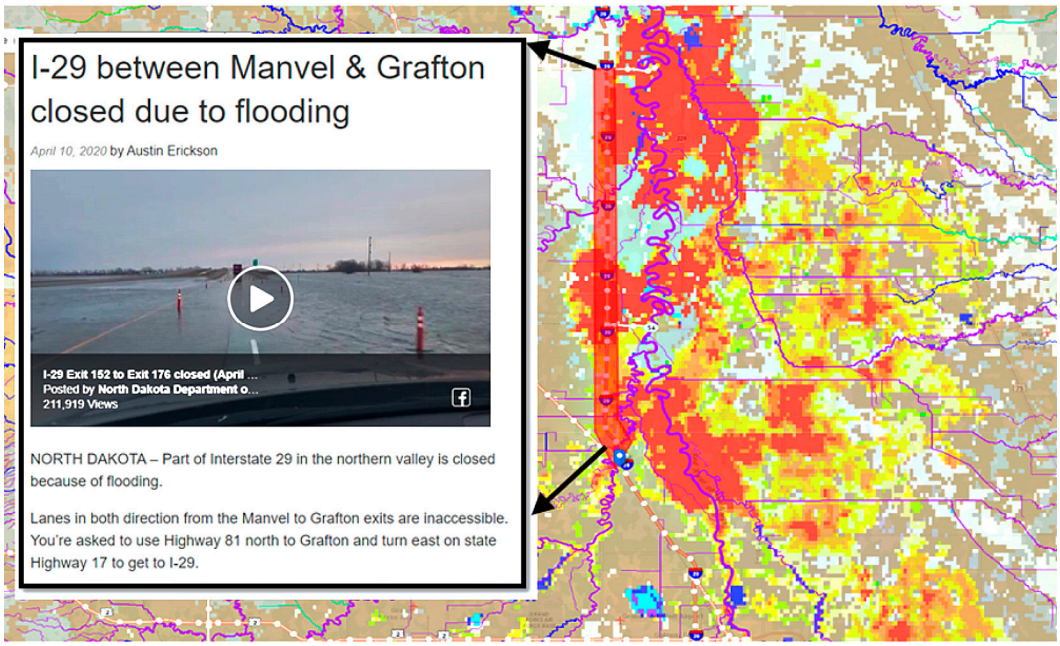

Figure 6. VIIRS 5-day (April 7–11) composite flood product in April 2020 (the color scale is the same as Figures 4 and 5. Courtesy of Dave Jones at the Storm Center).

The Red River passes through some of North Dakota's most populated areas. While the ABI flood products are updated hourly, the ABI's spatial resolution of 1 km may smooth out the spatial extent of potentially impactful floodwaters. VIIRS offers the same imagery at the finer resolution of 375 m, but at the expense of producing only one image during the daytime, which requires a clear sky to provide useful information. The VIIRS 5-day composite flood map can remove cloud contamination, and is shown in Figure 6. It confirmed higher percentage values of flooding water in the same areas of interest. Although our algorithms have been intensively validated and evaluated [33], ground observations of the I-29 road closure due to flooding in North Dakota can also validate our flood product.

High resolution satellite imagery, down to 10-m from Sentinel-2, can be obtained from the Sentinel-Hub EO Browser [38]. A timely, cloud-free pass from the Sentinel-2 satellite over the area of interest is available for comparison and evaluation (Figure 7). As shown in Figure 7, compared to Figure 6, in the VIIRS flood map, a high percentage of floodwater fraction (>90% in red color) corresponds to deep water, in the dark blue color in the Sentinel imagery, while lower percentage values (60~80% in yellow color) correspond to shallow water, in the lighter blue color in the Sentinel image. Sentinel-2 imagery hinted that the spatial distribution of these floodwaters was close to the ABI [Figure 5c,d] and VIIRS (Figure 6) flood extent areas, confirming that impactful flooding would be possible there.

Figure 7. Sentinel-2 Short wave infrared composite (SWIR) imagery on 10 April 2020.

4. Discussion

The large spatial coverage and frequent revisits of coarse-to-moderate resolution operational satellite imagery, such as the VIIRS onboard the SNPP and the current and future JPSS series, and the ABI onboard the GOES-R series, have advantages in flood detection and monitoring over large areas. In high latitude regions, multiple observations are available from polar-orbiting satellites during the day, which can help dynamically monitor and predict floods due to ice jams. In the cases of this study, floods were due to ice jams and snowmelt, but the procedures and algorithms can be applied to warm season floods due to heavy rainfall as well. The VIIRS and GOES-R flood products are routinely generated at the Space Science and Engineering Center (SSEC), University of Wisconsin, Madison, and the Geographic Information Network of Alaska (GINA) at the University of Alaska, which have access to directly broadcast VIIRS and GOES-R data. The VIIRS and GOES-R near-real time (NRT) flood products can be accessed in Real Earth and Advanced Weather Interactive Processing System (AWIPS)-II. The latest flood products are available in NRT from Real Earth [39]. The archived global flood products can be available from the JPSS Proving Ground Global Flood Products Archive [40]. Relatively few studies have been undertaken that apply models in river ice forecasting. Currently, numerical models for ice floods were developed for simulating ice jam flood for several specific rivers, but they were seldom used for the prediction of ice jam locations and floods [8–11,41]. One big advantage of the VIIRS and GOES-R flood products, including snow and ice information, is that they can be generated automatically at near-real time, are not limited to specific rivers, and can be used for the dynamic monitoring and prediction of floods due to ice jams and snowmelt all over the globe. Thick ice can rapidly break up under the condition of warm temperature. Morales-Marín et al. [42] found that ice breakup occurred when the simulated water temperature (Tw) was above 5 °C. In most high latitude regions, if there is significant snow cover, warm temperatures will not only melt ice, but also melt snow, and can cause ice jam flooding. By combination with temperature data, it is expected that satellite-based flood products will allow more quantitative predictions regarding the breakup timing and locations of floods due to ice jams and snowmelt.

5. Conclusions

In this study, satellite imagery from VIIRS and ABI flood products provided excellent details of river and overland flooding. Even though the spatial resolution of GOES-R is relatively coarse

(1 km), its highest temporal resolution imagery, such as the ABI, was a good starting point in searching for floodwaters over a large area. In providing the highest flood extent signals, as well as multi-day composite flood products from higher spatial resolution imagery, VIIRS has proven to be a good approach in pinpointing areas of interest to target in more detail. In high latitude regions, conventional observations are usually sparse, while polar-orbiting satellite observations are available at multiple times in the day, and show the advantages of dynamic monitoring and prediction of floods due to ice jam. Comparisons via visual inspection with the false color images, high resolution satellite imagery and ground observations showed good agreement. With the efforts and demonstrations of this study, the VIIRS and GOES-R flood products can provide dynamic monitoring and prediction of floods due to ice jams and snowmelt for wide-end users.

Author Contributions: Methodology, S.L. and D.S.; software, S.L.; validation, S.L. and D.S.; formal analysis, S.L. and D.S.; investigation, S.L. and D.S.; data curation, S.L.; writing—original draft preparation, D.S.; writing—review and editing, D.S., S.L., M.D.G., D.T.L., W.S. and L.Z.; visualization, S.L. and D.S.; supervision, M.D.G., D.T.L., W.S., and L.Z.; project administration, W.S. and L.Z.; funding acquisition, M.D.G., D.T.L., and L.Z. All authors have read and agreed to the published version of the manuscript.

Funding: This work is supported by NOAA JPSS and GOES-R Programs under grant #NA12NES4400008. The contents are solely the opinions of the authors and do not constitute a statement of policy, decision, or position on behalf of NOAA or the U. S. Government. We thank the reviewers and the editors for their helpful and constructive comments!

Acknowledgments: This work is supported by NOAA JPSS and GOES-R Programs. The constructive and helpful comments from the reviewers and editors are greatly appreciated!

Conflicts of Interest: The authors declare no conflict of interest.

References

1. Sun, Z.; Sui, J. Calculation of water level in a river reach with frazil ice jam. In Proceedings of the 10th IAHR Symposium on Ice Problems, Espoo, Finland, 20–23 August 1990; Volume II, pp. 756–765.
2. Tropeano, D.; Turconi, L. Geomorphic classification of alpine catchments for debris-flow hazard reduction. In Proceedings of the International Conference on Debris-Flow Hazards Mitigation: Mechanics, Prediction and Assessment, Davos, Switzerland, 10–12 September 2003; Millpress Science Pub: Rotterdam, Switzerland, 2003; Volume 2, pp. 1221–1232.
3. Goldberg, M.D.; Cikanec, H.A.; Zhou, L.; Price, J. The join polar satellite system. In *Comprehensive Remote Sensing*; Liang, S., Ed.; Elsevier: New York, NY, USA, 2017; p. 108. ISBN 9780128032206.
4. Wang, C. Numerical Modelling of Ice Floods in the Ning-Meng Reach of the Yellow River Basin. Dissertation, 2017. Available online: https://www.un-ihe.org/sites/default/files/2017_unesco-ihe_phd_thesis_wang_i.pdf (accessed on 4 June 2020).
5. Marchil, L.; Chiarle, M.; Mortara, G. Climate changes and debris flows in periglacial areas in the Italian Alps. In *From Headwaters to the Ocean: Hydrological Changes and Watershed Management*; Taniguchi, M., Burnett, W.C., Fukushima, Y., Haigh, M., Umezawa, Y., Eds.; Taylor and Francis: London, UK, 2009; pp. 111–113.
6. Nigrelli, G.; Fratianni, S.; Zampollo, A.; Turconi, L.; Chiarle, M. The altitudinal temperature lapse rates applied to high elevation rockfalls studies in the Western European Alps. *Theor. Appl. Climatol.* **2018**, *131*, 1479–1491. [CrossRef]
7. Turconi, L.; De, S.K.; Tropeano, D.; Savio, G. Slope failure and related processes in the Mt. Rocciamelone area (Cenischia valley, Western Italian). *Geomorphology* **2010**, *114*, 115–128. [CrossRef]
8. Thériault, I.; Saucet, J.-P.; Taha, W. Validation of the mike-ice model simulating river flows in presence of ice and forecast of changes to the ice regime of the romaine river due to hydroelectric project. In Proceedings of the 20th IAHR International Symposium on Ice, Lahti, Finland, 14–17 June 2010.
9. Chen, F.; Shen, H.T.; Jayasundara, N. A one-dimensional comprehensive river ice model. In Proceedings of the 18th International Association of Hydraulic Research Symposium on ice, Sapporo, Japan, 28 August–1 September 2006.
10. Blackburn, J.; She, Y. A comprehensive public-domain river ice process model and its application to a complex natural river. *Cold Reg. Sci. Technol.* **2019**, *163*, 44–58. [CrossRef]
11. Lindenschmidt, K.-E. RIVICE—A non-proprietary, open-source, one-dimensional river-ice and water-quality model. *Water* **2017**, *9*, 314. [CrossRef]

12. Yu, K.X.; Zhang, X.; Li, L.; Zhan, B.; Qin, Y.; Su, Q. Probability prediction of peak breakup water level through vine copulas. *Hydrol. Process.* **2019**, *33*, 962–977. [CrossRef]
13. Sheng, Y.; Gong, P.; Xiao, Q. Quantitative dynamic flood monitoring with NOAA AVHRR. *Int. J. Remote Sens.* **2001**, *22*, 1709–1724. [CrossRef]
14. Sun, D.; Yu, Y.; Goldberg, M. Deriving water fraction and flood maps from MODIS images using a decision tree approach. *IEEE J. Sel. Top. Appl. Earth Observ. Remote Sens.* **2011**, *4*, 814–825. [CrossRef]
15. Sun, D.; Yu, Y.; Zhang, R.; Li, S.; Goldberg, M. Towards operational automatic flood detection using EOS/MODIS data. *Photogramm. Eng. Rem. Sens.* **2012**, *78*, 637–646. [CrossRef]
16. Li, S.; Sun, D.; Yu, Y.; Csiszar, I.; Stefanidis, A.; Goldberg, M. A New Shortwave Infrared (SWIR) Method for Quantitative Water Fraction Derivation and Evaluation with EOS/MODIS and Landsat/TM data. *IEEE Trans. Geosci. Remote Sens.* **2012**, *51*, 1852–1862. [CrossRef]
17. Bates, P.D.; Wilson, M.D.; Horritt, M.S.; Mason, D.C.; Holden, N.; Currie, A. Reach scale flood plain inundation dynamics observed using airborne synthetic aperture radar imagery: Data analysis and modeling. *J. Hydrol.* **2006**, *328*, 306–318. [CrossRef]
18. Sippel, S.J.; Hamilton, S.K.; Melack, J.M.; Choudhury, B.J. Determination of inundation area in the Amazon river floodplain using the SMMR 37 GHz polarization difference. *Remote Sens. Environ.* **1994**, *48*, 70–76. [CrossRef]
19. Jin, Y.Q. Flooding index and its regional threshold value for monitoring floods in China from SSM/I data. *Int. J. Remote Sens.* **1999**, *20*, 1025–1030. [CrossRef]
20. Tanaka, M.; Sugimura, T.; Tanaka, S.; Tamai, N. Flood drought cycle of Tonle Sap and Mekong Delta area observed by DMSP-SSM/I. *Int. J. Remote Sens.* **2003**, *24*, 1487–1504. [CrossRef]
21. Temimi, M.; Leconte, R.; Brissette, F.; Chaouch, N. Flood and soil wetness monitoring over the Mackenzie River Basin using AMSR-E 37 GHz brightness temperature. *J. Hydrol.* **2007**, *333*, 317–328. [CrossRef]
22. Zheng, W.; Liu, C.; Wang, Z.X.; Xin, Z.B. Flood and waterlogging monitoring over Huaihe River Basin by AMSR-E data analysis. *Chin. Geogr. Sci.* **2008**, *18*, 262–267. [CrossRef]
23. Beaton, A.; Whaley, R.; Corston, K.; Kenny, F. Identifying historic river ice breakup timing using MODIS and Google earth engine in support of operational flood monitoring in northern Ontario. *Remote Sens. Environ.* **2019**, *224*, 352–364. [CrossRef]
24. Lindenschmidt, K.E.; Li, Z. Radar scatter decomposition to differentiate between running ice accumulations and intact ice covers along rivers. *Remote Sens.* **2019**, *11*, 307. [CrossRef]
25. Lindenschmidt, K.E.; Rokaya, P.; Das, A.; Li, Z.; Richard, D. A novel stochastic modelling approach for operational real-time ice-jam flood forecasting. *J. Hydrol.* **2019**, *575*, 381–394. [CrossRef]
26. JPSS Proving Ground Portfolio, 2018–2021. Available online: https://www.jpss.noaa.gov/assets/pdfs/2018%20JPSS%20PGRR%20Portfolio.pdf (accessed on 4 June 2020).
27. Xian, G.; Homer, C.; Dewitz, J.; Fry, J.; Hossain, N.; Wickham, J. The change of impervious surface area between 2001 and 2006 in the conterminous United States. *Photogramm. Eng. Remote Sens.* **2011**, *77*, 758–762.
28. Rabus, B.; Eineder, M.; Roth, A.; Bamler, R. The shuttle radar topography mission—A new class of digital elevation models acquired by spaceborne radar. *Photogramm. Remote Sens.* **2003**, *57*, 241–262. [CrossRef]
29. Carroll, M.; Townshend, J.; DiMiceli, C.; Noojipady, P.; Sohlberg, R. A New Global Raster Water Mask at 250 Meter Resolution. *Int. J. Dig. Earth* **2009**, *2*, 291–308. [CrossRef]
30. Liang, Y.-L.; Colgan, W.; Lv, Q.; Steffen, K.; Abdalati, W.; Stroeve, J.; Gallaherb, D.; Bayou, N. A decadal investigation of supraglacial lakes in West Greenland using a fully automatic detection and tracking algorithm. *Remote Sens. Environ.* **2012**, *123*, 127–138. [CrossRef]
31. Johansson, A.M.; Brown, I.A. Adaptive classification of supraglacial lakes on the West Greenland ice sheet. *IEEE J. Sel. Top. Appl. Earth Obs. Remote Sens.* **2013**, *6*, 1998–2007. [CrossRef]
32. Lesson, A.; Leeson, A.; Shepherd, A.; Sundal, A.V.; Johansson, A.M.; Selmes, N.; Briggs, K.; Hogg, A.E.; Fettweis, X. A comparison of supraglacial lake observations derived from MODIS imagery at the western margin of the Greenland ice sheet. *J. Glaciol.* **2013**, *59*, 1179–1188. [CrossRef]
33. Li, S.; Sun, D.; Goldberg, M.D.; Sjoberg, B.; Santek, D.; Hoffman, J.P.; DeWeese, M.; Restrepo, P.; Lindsey, S.; Holloway, E. Automatic near real-time flood detection using Suomi-NPP/VIIRS data. *Remote Sens. Environ.* **2017**, *204*, 672–689. [CrossRef]
34. Li, S.; Sun, D.; Yu, Y. Automatic cloud-shadow removal from flood/standing water maps using MSG/SEVIRI imagery. *Int. J. Remote Sens.* **2013**, *34*, 5487–5502. [CrossRef]

35. Li, S.; Sun, D.; Goldberg, M.D.; Sjoberg, W. Object-based automatic terrain shadow removal from SNPP/VIIRS flood maps. *Int. J. Remote Sens.* **2015**, *36*, 5504–5522. [CrossRef]
36. Shepard, M.K.; Campbell, B.A.; Bulmer, M.H.; Farr, T.G.; Gaddis, L.R.; Plaut, J.J. The roughness of natural terrain: A planetary and remote sensing perspective. *J. Geophys. Res.* **2001**, *106*, 32777–32795. [CrossRef]
37. Goldberg, M.; Li, S.; Goodman, S.; Lindsey, D.; Sjoberg, D.; Sun, D. Contributions of Operational Satellites in Monitoring the Catastrophic Floodwaters Due to Hurricane Harvey. *Remote Sens.* **2018**, *10*, 1256. [CrossRef]
38. The Sentinel-Hub EO Browser. Available online: https://apps.sentinel-hub.com/eo-browser (accessed on 4 June 2020).
39. VIIRS Flood Products in Near Real Time. Available online: http://wms.ssec.wisc.edu/s/A8LT (accessed on 4 June 2020).
40. JPSS Proving Ground Global Flood Products Archive. Available online: https://jpssflood.gmu.edu/ (accessed on 4 June 2020).
41. Rokaya, P.; Morales-Marin, L.; Lindenschmidt, K.E. A physically-based modelling framework for operational forecasting of river ice breakup. *Adv. Water Resour.* **2020**, *139*, 103554. [CrossRef]
42. Morales-Marín, L.A.; Sanyal, P.R.; Kadowaki, H.; Li, Z.; Rokaya, P.; Lindenschmidt, K.E. A hydrological and water temperature modelling framework to simulate the timing of river freeze-up and ice-cover breakup in large-scale catchments. *Environ. Model. Softw.* **2019**, *114*, 49–63. [CrossRef]